High Sensitivity Balloon-Like Sensor Based on Twin-Core and Twin-Hole Fiber

Jing Zhang, Yongqian Li, and Guozhen Yao

***Abstract*—An all-fiber Mach–Zehnder interferometric (MZI) sensor for measuring temperature and refractive index (RI) is proposed and experimentally demonstrated. A high sensitivity balloon-like mode interferometer is fabricated with a twin-core and twin-hole fiber (TCTHF). The variations in ambient temperature and RI cause changes in phase differences between the modes, leading to shifts in the interference spectrum. The two resonance dip wavelength shifts within the spectrum are used to investigate the temperature and RI characteristics of the sensor. Experimental results show that the two dips have different responses to temperature and RI, indicating that the sensor can realize simultaneous measurement of temperature and RI. The obtained maximum sensing sensitivities are 0.051 nm/°C and 423.168 nm/RIU. The proposed sensor has potential applications in physical, biological, and chemical sensing owing to its high sensitivity, low cost, and small size.**

***Index Terms*—Mach–Zehnder interferometric, Multimode fiber, Refractive index measurement, Twin-core and twin-hole fiber, Temperature measurement.**

I. Introduction

OPTICAL fiber sensors have been widely used in the sensing applications of various physical, biological, and chemical measurements. Numerous optical fiber sensors based on different structures have been proven to be capable of measuring several parameters in recent years. Among these parameters, temperature and refractive index (RI) are the most important in many applications. A variety of optical fiber temperature or RI sensors, such as optical fiber interferometer sensor [1]–[4], surface plasmon resonance optical fiber sensor [5], and optical fiber grating sensor [6]–[9] have been developed. Among these optical fiber temperature and RI sensors, optical fiber sensors based on different coupling structures, such as single–mode fiber (SMF)–multimode fiber(MMF)–SMF structure [10], [11], SMF–tapered Bragg grating–SMF [12], [13], special optical fiber cascade [14], [15], fiber transverse offset splicing [16], and combined structures [17]–[24] have attracted increasing attention in frontier fields, such as physics, biology, and chemistry. The simultaneous measurement of multiple parameters using optical fiber sensors is widely used in complex environmental monitoring.

Zheng *et al.* [18] developed a sensor comprising a few-mode fiber and two spherical structures. The spherical structure acts as a coupler, which can excite high-order modes and couple back the high-order modes and cladding modes into the optical fiber. This sensor can simultaneously measure the temperature and RI. Within the ranges of 25 °C–80 °C and 1.335–1.398, the sensitivities of temperature and RI are 0.054 nm/°C and 27.77 nm/RIU, respectively. Dong *et al.* [19] devised a D-type fiber structure combined with fiber Bragg grating (FBG) to measure the temperature and RI. The sensitivities of temperature and RI are 28.7 pm/°C and 31.79 nm/RIU, respectively. Shi *et al.* [20] proposed a Sagnac ring based on long–period grating (LPG) and polarization–maintaining fiber (PMF) to simultaneously measure temperature and RI. The sensitivities of temperature and RI of LPG are 0.201 nm/°C and 8.36 nm/RIU, respectively, whereas the sensitivities of the Sagnac ring are 1.06 nm/°C and 23.068 nm/RIU, respectively. Although both the temperature and RI can be measured simultaneously by these sensors, the sensitivity of RI is relatively low. Zhao *et al.* [21] proposed an interference structure composed of Sagnac loop mirror and balloon–like interferometer, which is used to measure temperature and RI at the same time. A segment of PMF is embedded into the Sagnac loop structure to form a Sagnac loop interferometer. The balloon–like structure is built with a bent SMF to form a mode interferometer. Experimental results show that the sensitivities of the temperature and RI can reach up to 1.7 nm/°C and 218.56 nm/RIU. The sensitivities are improved compared with the previous ones. However, the sensor structure reported in this literature is fabricated in series with Sagnac loop and MZI, which will increase the size of the sensor and is not suitable for miniaturization measurement.

In addition to the sensing structures for simultaneous measurement of temperature and RI, other structures of sensors for measuring curvature or transverse load have also been proposed. Yin *et al.* [22] proposed an intensity–modulated bend sensor by using a SMF–twin–core fiber (TCF)–SMF structure. The sensor was created by splicing a segment of TCF between two segments of SMF. The diameters of the two cores are 5.96 μm and 7.19 μm, respectively, and the distance between the centers of the cores is 14.8 μm. The curvature is measured by coupling the modes between the cores, and the intensity–modulated method is applied

Manuscript received May 27, 2022; accepted June 9, 2022. Date of publication June 13, 2022; date of current version June 22, 2022. This work was supported in part by the National Natural Science Foundation of China under Grants 61775057 and 61377088, in part by the S&T Program of Hebei, China under Grant SZX2020034, in part by the Natural Science Foundation of Hebei Province of China under Grant F2019502112, and in part by the Fundamental Research Funds for the Central Universities, China under Grant 2017MS108. *(Corresponding author: Jing Zhang.)*

The authors are with the Department of Electronic and Communication Engineering, North China Electric Power University, Hebei Key Laboratory of Power Internet of Things Technology, Baoding, Hebei 071003, China (e-mail: 22456188@qq.com; 51550779@ncepu.edu.cn; 51551347@ncepu.edu.cn).

Digital Object Identifier 10.1109/JPHOT.2022.3182751

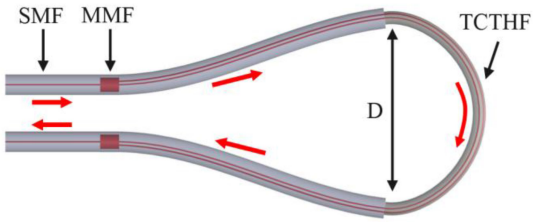

Fig. 1. Schematic diagram of sensor structure.

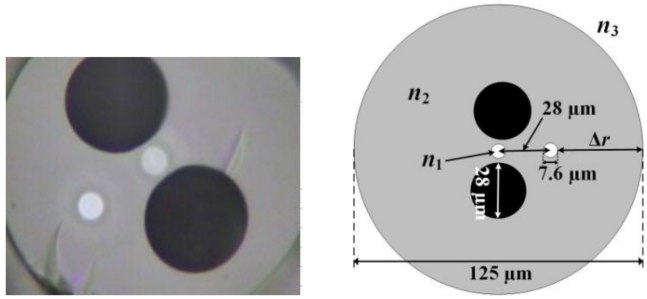

Fig. 2. Cross section of TCTHF: (a) micrograph and (b) schematic diagram.

for the bend measurement. The sensor achieves a sensitivity of 0.671 /m^{-1} and a resolution of 0.003 m^{-1} in the range of 0 to 1.25 m^{-1}. However, the precision of curvature measurement using light intensity is relatively low, and the phase ambiguity is easy to occur in a large range of curvature measurement. He *et al.* [23] proposed a temperature–insensitive directional transverse load sensor based on an FBG inscribed in a segment of dual side-hole fiber (DSHF). The resulting FBG transmission dip features two individual Bragg wavelengths corresponding to transverse electric and transverse magnetic modes, respectively, induced by the birefringence in the DSH-FBG. The birefringence changes in case the DSHF is subjected to transverse loads, leading to a wavelength separation, which exhibits a different sensitivity to the transverse loads applied in different directions. The load sensitivity exhibited two maxima and two minima in a polar coordinate system, achieving a maximum value of 699 pm/(N/mm) for transverse load applied along the slow axis and a minimum value of 285 pm/(N/mm) for transverse load applied along the fast axis. Tapered stretching and bending techniques have been used in many sensor structures in recent years to achieve high-sensitivity measurement [24], [25]. However, tapered optical fiber sensors are considerably fragile. Thus, the use of these sensors in practical applications is difficult.

In this paper, an all–fiber high sensitivity balloon–like mode interferometer based on twin–core and twin–hole fiber (TCTHF) is proposed, and the temperature and RI characteristics are analyzed theoretically and verified experimentally. The experimental results show that the temperature sensitivity is 0.051 nm/°C in the range of 25°C–75°C, and the RI sensitivity is 423.168 nm/RIU in the range of 1.3423–1.3478. The proposed sensor has the characteristics of high sensitivity, simple structure, strong robustness and low price.

II. Sensor Fabrication and Configuration

The schematic diagram of the sensor structure is shown in Fig. 1. The MMF (YOFC Optical Fiber Company) is fused at the two ends of the TCTHF. The core and cladding diameters of MMF are 105 μm and 125 μm, respectively. The two ends of the MMF are fused with the SMF (YOFC Optical Fiber Company), with a core and cladding diameter of 8.2 μm and 125 μm, respectively, as the input and output fibers. The sensing structure is bent into a balloon-like shape. The diameter is defined as D, as illustrated in Fig. 1.

The TCTHF in the sensor consists of a central core, a side core and two air holes. The micrograph of TCTHF cross section is shown in Fig. 2(a), and the schematic diagram of TCTHF cross section is shown in Fig. 2(b). The two cores has the same diameter of 7.6 μm and are asymmetrically located. One core is along the central axis, and the distance between the centers of the cores is 28 μm. The RI of center core and side core is n_1, and the value is 1.4510. The RI of fiber cladding is n_2, and the RI difference between the core and cladding is 0.0042. The diameter of the air hole is 28 μm, and the RI is 1. The ambient RI is n_3.

In the process of fabricating the sensor, first, both ends of TCTHF are spliced with two segments of MMF. Manual alignment is adopted when splicing MMF and TCTHF. After the MMF core is aligned with the TCTHF center core, the splicer is operated to complete splicing. Due to the existence of air holes, part of the air holes collapses, and the insertion loss of the fusion point is about 1.3 dB. Second, both ends of MMF are spliced with two segments of SMF as input and output optical fibers. The splicing is automatically implemented by using the standard SMF splicing mode. The fiber alignment method is selected to be core–to–core. The splicer can automatically align the SMF core with the MMF core and complete the splicing. The insertion loss of the fusion point is about 0.7 dB. After splicing, a section of the TCTHF is placed in hydrofluoric acid for 30 minutes to remove part of the cladding and let the side core be mostly exposed. The thickness of the remained cladding can be controlled by changing the etching temperature or etching time. When the etching reaches the specified time, one end of the sensor structure is bonded to the glass substrate with UV adhesive. Then, the TCTHF is bent to a specified radius and the other end of the sensor is also bonded to the same glass substrate with UV adhesive. Although the splicing method is easy to perform, the fiber needs to cut and spliced carefully. Splicing loss can reduce the coupling ratio, which influences the fringe visibility and transmission loss of the interference spectrum.

When light is launched into the MMF through the lead–in SMF at the spliced point, high–order modes are excited to transmit in the core of MMF due to the mode mismatch. The fundamental mode at the spliced point of MMF and TCTHF is coupled back to the central core and the side core. Part of the fundamental and higher order modes is transmitted in the air hole and cladding. A part of light will be free from the constraint of the side core due to the fiber bending and penetrate into the

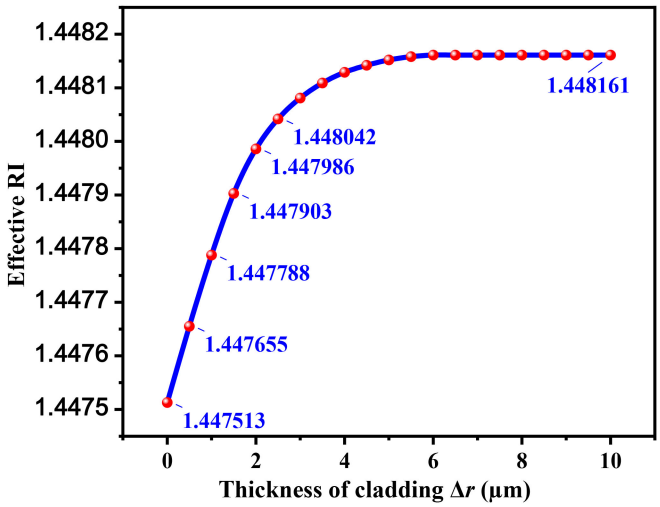

Fig. 3. Simulated effective RI of the fundamental mode of the side core versus the cladding thickness with an interval of 0.5 μm.

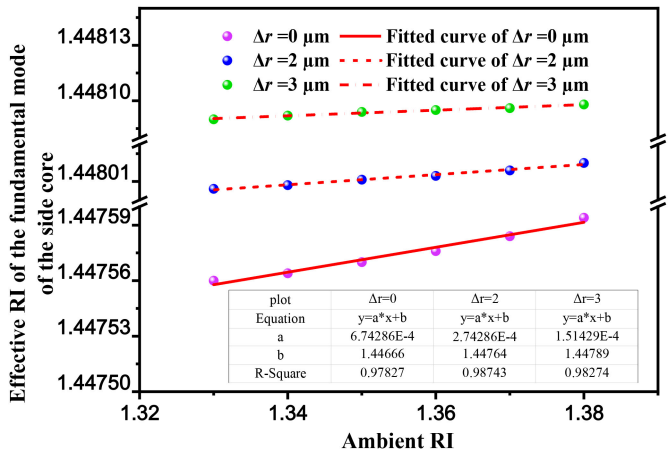

Fig. 4. Relationships between effective RI of the fundamental mode of side core and ambient RI under different Δr.

cladding when the light propagates into the balloon-like bending section. After passing through the bending region, the cladding modes will couple back to the side core. At the spliced point of MMF and lead–out SMF, the cladding modes and fundamental mode of the side core interfere with the fundamental mode of the center core. These modes with different effective RI and transmission path interfere at the output of the sensor. As the effective RI of side core cladding modes and fundamental mode depend on the ambient RI, the change of ambient RI will affect the phase difference between these modes, which leads to the spectral shift of the transmission spectrum.

III. Theoretical Analysis

For the TCTHF used in the sensor structure, no coupling is observed between the central core and the side core due to the large separation between the two cores. We mainly focus on the analysis of the propagation characteristics of the side core because the central core mode are mostly unaffected by the ambient RI change.

The schematic diagram of cross section of TCTHF is shown in Fig. 2(b). The cladding radius is 62.5 μm, and Δr is the thickness of the side core cladding. The wave equations of electric field **E** and magnetic field **H** are expressed as:

$$\left[\nabla_t^2 + \left(\mathrm{n}^2\mathrm{k}_0^2 - \beta^2\right)\right] \begin{bmatrix} \boldsymbol{E} \\ \boldsymbol{H} \end{bmatrix} = 0, \tag{1}$$

where β represents the longitudinal propagation constant, $k_0 = 2\pi/\lambda$ is the wave number in vacuum, λ is the wavelength in vacuum, and n is the RI of optical fiber material. The analytical expression of the mode field is difficult to obtain. Therefore, numerical method (finite element method) is chosen for analyzing effective RI of the fundamental mode of the side core. The ambient RI is set to be 1, n_1 is set to be 1.4510, n_2 is set to be 1.4468, and the wavelength is set to be 1550 nm. The simulated effective RI of the fundamental mode of the side core with different Δr is shown in Fig. 3. The effective RI increases with Δr and changes rapidly when the thickness is less than 4 μm. When the thickness is greater than 6 μm, the effective RI does not change and remains stable. Therefore, if the cladding of the TCTHF is removed to the extent of $\Delta r < 4\ \mu m$, the fundamental mode of the side core is sensitive to the change of ambient RI.

In order to verify the effect of ambient RI on the effective RI of side core fundamental mode, the effective RI of side core fundamental mode with ambient RI is calculated. The thickness of the side core cladding is set to be 0 μm, 2 μm, and 3 μm, respectively. The relationships between effective RI and ambient RI are shown in Fig. 4. The sensitivity of fundamental mode effective RI change to ambient RI change can be expressed as $\Delta n_{eff}^{side}/\Delta\, n_3 = k$. It can be seen from Fig. 4, $k = 6.74 \times 10^{-4}$ at the condition of$\Delta r = 0\,\mu m$, $k = 2.74 \times 10^{-4}$ at the condition of$\Delta r = 2\mu$m, and $k = 1.51 \times 10^{-4}$ at the condition of $\Delta r = 3\,\mu$m. The fitting curve shows that with the decrease of Δr, the change of ambient RI has a greater influence on the effective RI of side core fundamental mode.

The mode effective RIs in the side core are sensitive to the ambient RI change, whereas the mode effective RIs in the central core are insensitive to the ambient RI change. The interference spectra between the central core and the side core can be used for RI measurement.

In order to verify the influence of fiber bending on evanescent field intensity, simulations are carried out to study the modes transmission and the normalized distribution of fundamental mode energy in the side core, and the results are shown in Fig. 5.

As can be seen from Fig. 5, when the optical fiber is bent, the energy of the fundamental mode in the core becomes smaller, part of the energy leaks into the cladding, and the evanescent field intensity enhances. The cladding modes will couple back to the side core after passing through the bending section.

From the above analysis, when Δr is less than $4\,\mu$m, the effective RIs of the side core fundamental mode and cladding modes are affected by the ambient RI, so the phase differences between the central core fundamental mode and other modes are affected by the change of ambient RI, leading to the spectral

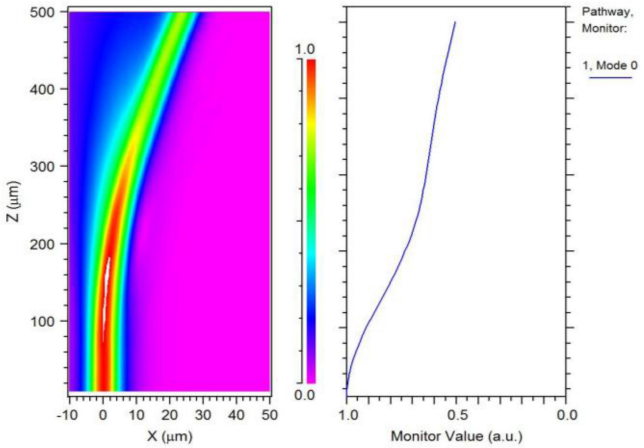

Fig. 5. Modes transmission under bending condition.

shift of the transmission spectrum. Assuming only two mode components interfere with each other, after the transmitted light passes through the balloon–like bending region, the transmission intensity can be expressed as [26]:

$$I_{out}(\lambda) = Icore(\lambda) + I_{other}(\lambda) + 2\sqrt{I_{core}(\lambda) \cdot I_{other}(\lambda)} \cdot \cos(\Delta\varphi), \quad (2)$$

where I_{core} and I_{other} are the intensity of the central core fundamental mode and other modes of which include side core fundamental mode and cladding modes, $\Delta\varphi$ is the phase difference between the central core mode and the other modes, and can be expressed as

$$\Delta\varphi = 2\pi\Delta n_{eff} L \Big/ \lambda_0 = \frac{2\pi}{\lambda_0}\left(n_{eff}^{core} - n_{eff}^{other}\right) L, \quad (3)$$

where λ_0 is the central wavelength, n_{eff}^{core} and n_{eff}^{other} are the effective RIs of central core fundamental mode and other modes, respectively. $\Delta\, n_{eff} = n_{eff}^{core} - n_{eff}^{other}$ is the effective RI difference between the central core fundamental mode and the other modes, and L is the length of the sensing unit. When is $(2\,m+1)$ π, the interference intensity is minimal, and the dip wavelength of the m–th order is

$$\lambda_m = 2\Delta n_{eff} L/(2m+1), m = 1, 2, \cdots. \quad (4)$$

When the ambient temperature and RI change, L and Δn_{eff} also change. In order to measure temperature and RI, two dip wavelengths with good sensitivity and linearity are selected as the characteristic wavelength, named as dip1 and dip2. The relationships between the wavelength change and the ambient parameters are as follows:

$$\begin{bmatrix} \Delta\lambda_1 \\ \Delta\lambda_2 \end{bmatrix} = \begin{pmatrix} k_{T1} & k_{R1} \\ k_{T2} & k_{R2} \end{pmatrix} \begin{bmatrix} \Delta T \\ \Delta R \end{bmatrix}, \quad (5)$$

where k_{T1} and k_{R1} are the temperature and RI sensitivity coefficients of dip1, k_{T2} and k_{R2} are the temperature and RI sensitivity coefficients of dip2, $\Delta\lambda_1$ and $\Delta\lambda_2$ are the wavelength changes of dip1 and dip2, and ΔT and ΔR are the changes of temperature and RI. By solving (5), we can obtain:

$$\begin{bmatrix} \Delta T \\ \Delta R \end{bmatrix} = \frac{1}{D}\begin{pmatrix} k_{R2} & -k_{R1} \\ -k_{T2} & k_{T1} \end{pmatrix} \begin{bmatrix} \Delta\lambda_1 \\ \Delta\lambda_2 \end{bmatrix}, \quad (6)$$

where $D = k_{T1}\, k_{R2} - k_{R1} k_{T2}$, and $D \neq 0$.

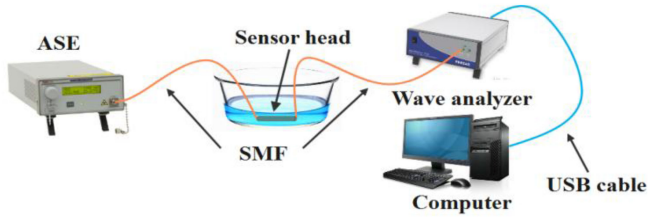

Fig. 6. Schematic diagram of experimental system.

IV. Experimental Results and Analysis

The balloon-like mode interferometers with different sensing lengths and bending diameters have different interference performances. The sensing length refers to the bare region of the fiber. The length of the optical fiber sensing part is measured before it is fabricated into a balloon-like interference structure. The sensing length should be chosen as small as possible to make the intensity change as a linear relationship. However, the curvature will be very small when the optical fiber sensing length is too small. Thus, the sensing length of the coating–stripped is selected to be about 25 mm. A cladding thickness of 1.5 μm and a bending radius of 15 mm are selected for the balloon-like structure. The sensing structure is adhered to the glass substrate by UV adhesive to ensure that the sensor head is fixed.

Schematic diagram of experimental system is shown in Fig. 6. The two ends of the sensor are connected to an amplified spontaneous emission source (ASE) with a wavelength range of 1510–1590 nm and a wave analyzer (1500S wave analyzer, Finisar Company) with a spectral resolution of 0.01 nm. The interference spectrum of the sensor is collected by the wave analyzer, and displayed, stored and analyzed by a computer.

A. Temperature Experiment

The temperature sensitivity of the sensor is investigated by putting it into a constant temperature device whose temperature can be adjusted. The accuracy of the device is 0.1°C. The photo of experimental system is shown in Fig. 7.

The temperature is raised from 25°C to 75°C, and the data are recorded every 10°C. In order to ensure the accuracy of measurement, the data are recorded after the temperature reaches the set value for 5 minutes. Transmission spectra at different temperatures are shown in Fig. 8. With the increase of temperature, the spectral shape and interference modes of transmission spectra remain unchanged. The whole spectrum moves towards the long wavelength direction.

The temperature experimental process was repeated 6 times. After averaging the results of 6 measurements, the average was subtracted from each measurement to calculate the repeatability error. The result is shown in Fig.9. It marks each dip fluctuation with a minimum repeatability error of 0.05 pm and a maximum

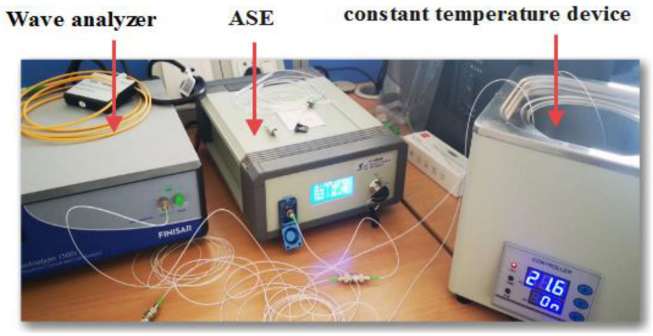

Fig. 7. Photo of experimental system.

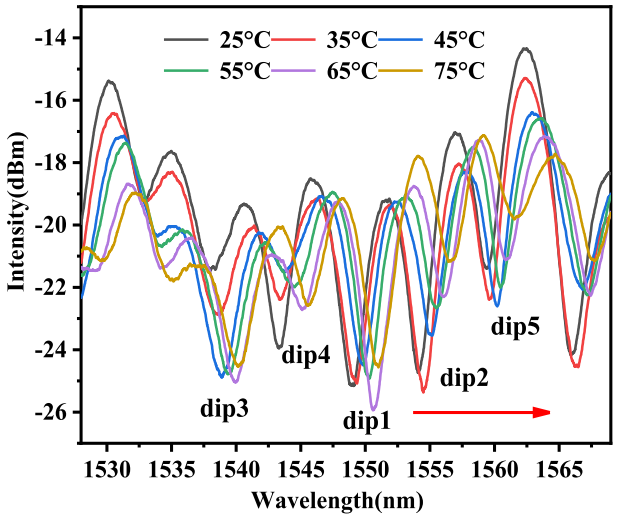

Fig. 8. Transmission spectra at different temperatures.

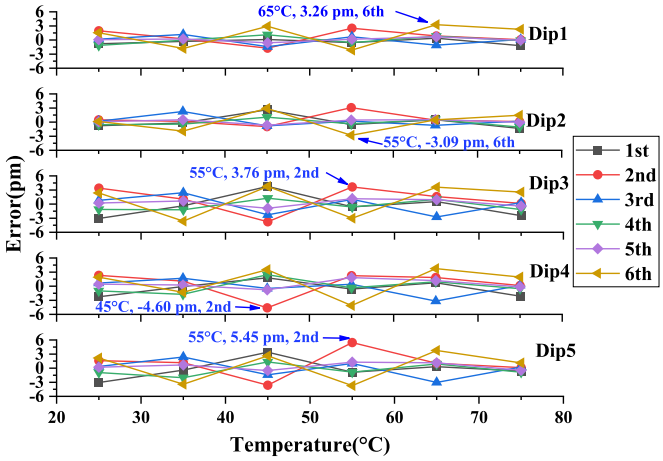

Fig. 9. Repeatability error of dips in the process of temperature change.

repeatability error of 5.45 pm. The repeatability error of each temperature point of the dip was small, and the fluctuation range was narrow, which meets the requirement for practical applications.

In order to analyze the origin and intensity distribution of interference modes, the transmission spectra in Fig.8 are Fourier

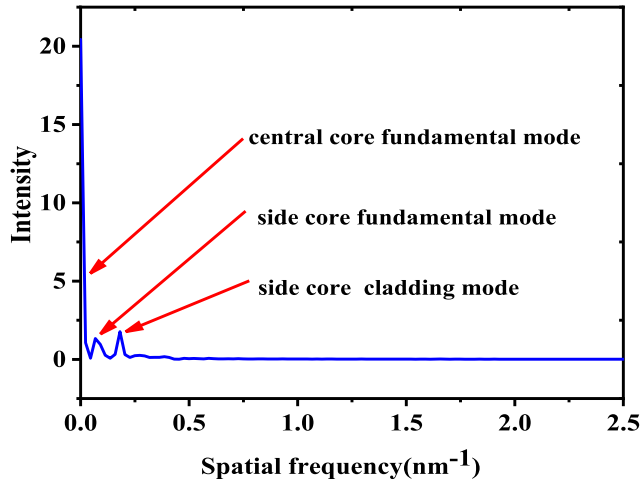

Fig. 10. Spatial spectral analysis.

transformed to get the spatial frequency spectra, and the result is shown in Fig. 10. The dominant intensity peak at zero relates to the central core fundamental mode. The intensity is primarily distributed in the central core fundamental mode, the side core fundamental mode and the side core cladding mode. It can be seen from Fig.9 that the side core cladding mode and the central core fundamental mode are the main interference modes. There is also interference between central core fundamental mode and side core fundamental mode. The interference also involves side core fundamental mode and side core cladding mode, but it contains less intensity.

B. RI Experiment

The performance of the sensor in measuring RI is evaluated by immersing it in five concentrations of NaCl solutions with the RI ranging from 1.3423 to 1.3478. In accordance with the empirical formula of NaCl solution [27], NaCl solutions with concentrations of 5%, 6%, 7%, 8%, and 9% are prepared at a room temperature of 25°C, and their corresponding RI is 1.3423, 1.3435, 1.3449, 1.3463, and 1.3478, respectively, which are verified by using an Abbe refractometer. The sensing unit is cleaned before each NaCl solution is replaced to restore the sensing spectrum to its original state. The transmission spectra of the sensor in different concentrations of NaCl solution are measured and shown in Fig. 11. With the increase of the ambient RI, the spectral shape and interference modes of transmission spectra remain unchanged. The whole spectrum moves towards the long wavelength direction.

Similarly, the RI experimental process was repeated 6 times. After averaging the results of 6 measurements, the average was subtracted from each measurement to calculate the repeatability error. The result is shown in Fig.12. It marks each dip fluctuation with a minimum repeatability error of 0.15 pm and a maximum repeatability error of 7.22 pm. The repeatability error of some dips is slightly larger, which is caused by a certain change in room temperature during the experiment.

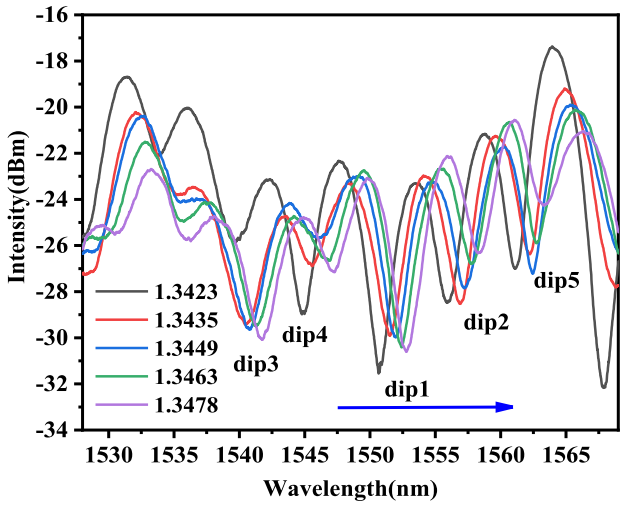

Fig. 11. Transmission spectra at different RIs.

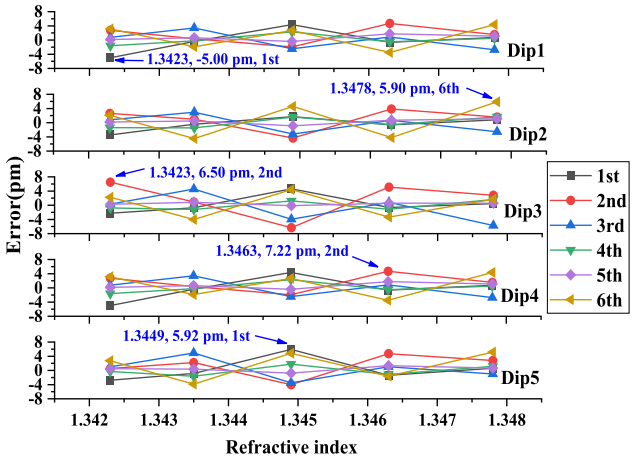

Fig. 12. Repeatability error of dips in the process of RI change.

C. Experimental Results Analysis

It can be seen from Figs. 8 and 10, the interference spectrum of the sensor contains multiple dips, so it is necessary to comprehensively consider the sensitivity and linearity of measurement. In order to select the appropriate dip wavelengths as the characteristic wavelengths, the sensitivity and linearity of the dips in the interference spectra are analyzed, and the results are shown in Table I.

Considering the sensitivity and linearity of dip wavelengths, dip1 and dip2 are selected for temperature and RI measurement. The relationships between temperature and wavelength are shown in Fig. 13. The dip1 and dip2 wavelengths have good linear relationships with temperature. The fitted temperature sensitivities of dips 1 and 2 are k_{T1}= 0.042 nm/°C and k_{T2}= 0.051 nm/°C, respectively.

The relationships between RI and wavelength are shown in Fig. 14. The dip1 and dip2 wavelengths have good linear relationships with ambient RI within the range of 1.3423–1.3478. The RI sensitivities of dip1 and dip2 are k_{R1}= 341.773 nm/RIU and k_{R2}= 423.168 nm/RIU, respectively.

TABLE I
SENSITIVITY AND LINEARITY ANALYSIS OF DIP WAVELENGTHS

DIP	Temperature		RI	
	Sensitivity (nm/°C)	R-Square	Sensitivity (nm/RIU)	R-Square
1	0.0419	0.9951	341.7727	0.9914
2	0.0507	0.9971	423.1680	0.9832
3	0.0395	0.9937	350.2245	0.9837
4	0.0416	0.9936	332.6682	0.9733
5	0.0431	0.9943	364.7435	0.9653

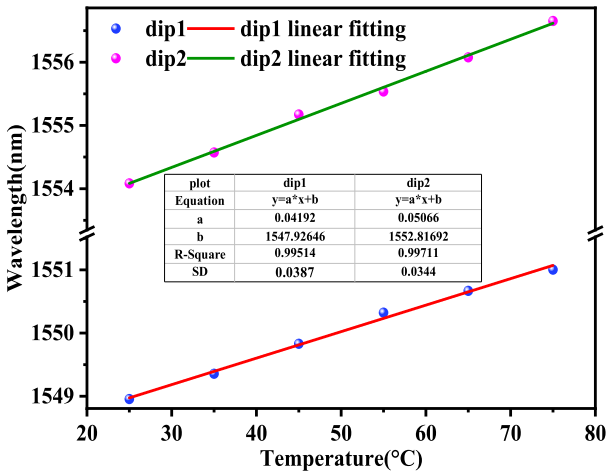

Fig. 13. Relationships between temperature and wavelength.

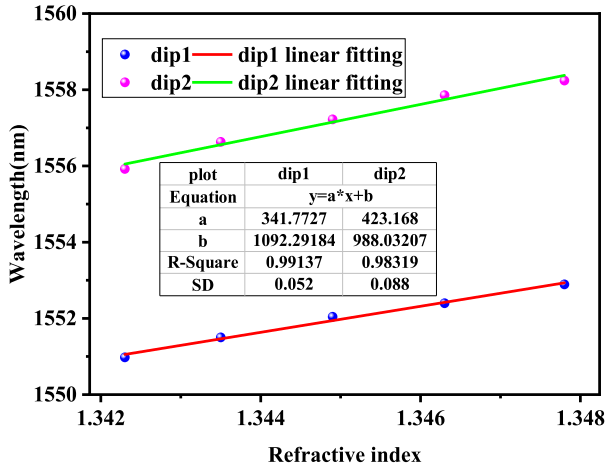

Fig. 14. Relationships between RI and wavelength.

In accordance with (6), the sensitivity matrix is

$$\begin{bmatrix} \Delta T \\ \Delta R \end{bmatrix} = \frac{1}{0.403} \begin{pmatrix} 423.168 & -341.773 \\ -0.051 & 0.042 \end{pmatrix} \begin{bmatrix} \Delta\lambda_1 \\ \Delta\lambda_2 \end{bmatrix} \quad (7)$$

In the actual measurement process, according to the changes of two wavelengths, the temperature and RI changes can be

obtained by (7). The sensitivity of the proposed sensor can be improved by properly choosing the remained cladding thickness that depends on the etching time and etching temperature. Therefore, the optimization of parameters, such as the bandwidth of light source and the cladding thickness near the side core, are important and should be investigated in detail to obtain better performance.

V. Conclusion

In this paper, a high sensitivity balloon–like sensor is proposed to measure the temperature and RI simultaneous. The sensor is composed of a segment of TCTHF, two small segments of MMFs and two segments of SMFs. The effect of the thickness of the TCTHF side core cladding on the effective RI of the side core fundamental mode is analyzed. The effect of optical fiber bending is simulated. The temperature and RI sensing characteristics of the sensor are theoretically analyzed and experimentally demonstrated. The experimental results show that the sensitivities of temperature and RI are 0.051 nm/°C and 423.168 nm/RIU, respectively. The sensitivity of the sensor can be adjusted by changing the cladding thickness of the side core, so that the proposed sensor can be used for either large-scale measurement or small–scale high–precision measurement. The proposed sensor features low cost, high sensitivity, simple configuration, and double-parameter measurement, which has great application potential in the field of physical, biological, and chemical sensing.

References

[1] J. R. Guzmán–Sepúlveda, R. Guzmán–Cabrera, and A. A. Castillo–Guzmán, "Optical sensing using fiber–optic multimode interference devices: A review of nonconventional sensing schemes," *Sensors*, vol. 21, no. 5, pp. 1–24, Mar. 2021, doi: 10.3390/s21051862.

[2] T. Liu, J. Wang, Y. Yang, Y. Lei, and S. Wang, "Splicing point tapered fiber Mach–Zehnder interferometer for simultaneous measurement of temperature and salinity in seawater," *Opt. Exp.*, vol. 27, no. 17, pp. 23905–23918, Aug. 2019, doi: 10.1364/OE.27.023905.

[3] Z. T. Lin, R. Lv, Y. Zhao, and H. Zheng, "High–sensitivity salinity measurement sensor based on no-core fiber," *Sensors Actuators A: Phys.*, vol. 305, no. 2, Apr. 2020, Art. no. 111947, doi: 10.1016/j.sna.2020.111947.

[4] H. Wan, J. Zhang, Q. Chen, Z. Wang, and Z. Zhang, "An active fiber sensor based on modal interference in few–mode fibers for dual-parameter detection," *Opt. Commun.*, vol. 481, no. 15, Feb. 2021, Art. no. 126498, doi: 10.1016/j.optcom.2020.126498.

[5] C. Liu *et al.*, "Mid–infrared surface plasmon resonance sensor based on photonic crystal fibers," *Opt. Exp.*, vol. 25, no. 13, pp. 14227–14237, Jun. 2017, doi: 10.1364/OE.25.014227.

[6] W. Zhang, W. Gao, Z. Tong, Y. Zhong, and H. Zhang, "Mach–Zehnder interferometer cascaded with FBG for simultaneous measurement of RI and temperature," *Opt. Commun.*, vol. 466, Jul. 2020, Art. no. 125624, doi: 10.1016/j.optcom.2020.125624.

[7] M. Zhang, Z. Hu, X. Wang, L. Xue, and L. Wang, "Power–type liquid–level sensor for high refractive index liquid based on long-period fiber grating," *Sensors Actuators A: Phys.*, vol. 324, Jun. 2021, Art. no. 112652, doi: 10.1016/j.sna.2021.112652.

[8] R. Fiorin, V. de Oliveira, H. J. Kalinowski, R. C. Kamikawachi, and I. Abe, "FBG–assisted micro-channel for refractive index measurements," *IEEE Photon. Technol. Lett.*, vol. 33, no. 1, pp. 35–38, Jan. 2021, doi: 10.1109/LPT.2020. 3043088.

[9] F. Ren, W. Zhang, Y. Li, Y. Lan, Y. Xie, and W. Dai, "The temperature compensation of FBG sensor for monitoring the stress on hole–edge," *IEEE Photon. J.*, vol. 10, no. 4, Aug. 2018, Art. no. 7104309, doi: 10.1109/JPHOT.2018.2858847.

[10] I. D. Villar, A. B. Socorro, J. M. Corres, F. J. Arregui, and I. R. Matias, "Optimization of sensors based on multimode interference in single–mode–multimode–single–mode structure," *J. Lightw. Technol.*, vol. 31, no. 22, pp. 3460–3468, Nov. 2013, doi: 10.1109/JLT.2013.2283943.

[11] Y. F. Chen, Q. Han, T. G. Liu, and X. Y. Lü, "Self-temperature-compensative refract meter based on single mode–multimode–single mode fiber structure," *Sensors Actuators B: Chem.*, vol. 212, pp. 107–111, Jun. 2015, doi: 10.1016/j.snb.2015.01.080.

[12] X. Liu, T. Wang, Y. Wu, Y. Gong, and Y. Rao, "Dual–parameter sensor based on tapered FBG combined with microfiber cavity," *IEEE Photon. Technol. Lett.*, vol. 26, no. 8, pp. 817–820, Apr. 2014, doi: 10.1109/LPT.2014.2306954.

[13] T. J. M. Martins, M. B. Marques, P. Roy, R. Jamier, S. Février, and O. Frazão, "Temperature-independent multi–parameter measurement based on a tapered Bragg fiber," *IEEE Photon. Technol. Lett.*, vol. 28, no. 14, pp. 1565–1568, Jul. 2016, doi: 10.1109/LPT.2016.2555300.

[14] B. Z. Zuo, X. Liang, X. R. Zhang, and T. H. Yin, "Detection of refractive index with a temperature–compensated MZI–based optical sensor using few–mode fiber," *IEEE Access*, vol. 9, pp. 158651–158659, Nov. 2021, doi: 10.1109/ACCESS.2021.313037.1.

[15] F. Wang, R. Wang, X. Wang, and Y. Liu, "Three–core fiber cascade asymmetric dual–taper robust structure for the simultaneous measurement of a mass concentration of a glucose solution and temperature," *Opt. Commun.*, vol. 461, Apr. 2020, Art. no. 125227, doi: 10.1016/j.optcom.2019.125227.

[16] S. Gao, C. G. Ji, Q. Y. Ning, W. C. Chen, and J. Q. Li, "High–sensitive Mach–Zehnder interferometric temperature fiber–optic sensor based on core–offset splicing technique," *Opt. Fiber Technol.*, vol. 56, May 2020, Art. no. 102202, doi: 10.1016/j.yofte.2020.102202.

[17] B. Y. Yang *et al.*, "High sensitivity balloon–like refractometric sensor based on single mode–tapered multimode-single mode fiber," *Sensors Actuators A: Phys.*, vol. 281, pp. 42–47, Oct. 2018, doi: 10.1016/j.sna.2018.08.034.

[18] Z. G. Tong, Y. M. Zhong, X. Wang, and W. H. Zhang, "Research on simultaneous measurement of refractive index and temperature comprising few mode fiber and spherical structure," *Opt. Commun.*, vol. 421, pp. 1–6, Aug. 2018, doi: 10.1016/j.optcom.2018.03.057.

[19] Y. Dong, S. Xiao, B. Wu, H. Xiao, and S. Jian, "Refractive index and temperature sensor based on D–shaped fiber combined with a fiber Bragg grating," *IEEE Sensors J.*, vol. 19, no. 4, pp. 1362–1367, Feb. 2019, doi: 10.1109/JSEN.2018.2880305.

[20] J. Shi, G. H. Su, D. G. Xu, and Y. Y. Wang, "A dual-parameter sensor using a long–period grating concatenated with polarization maintaining fiber in Sagnac loop," *IEEE Sensors J.*, vol. 16, no. 11, pp. 4326–4330, Jun. 2016, doi: 10.1109/JSEN.2016.2544305.

[21] Y. Zhao, X. Liu, R. Q. Lv, and Q. Wang, "Simultaneous measurement of RI and temperature based on the combination of Sagnac loop mirror and balloon-like interferometer," *Sens. Actuators B Chem.*, vol. 243, pp. 800–805, May 2017, doi: 10.1016/j.snb.2016.12.016.

[22] G. L. Yin, F. C. Zhang, B. J. Xu, J. He, and Y. P. Wang, "Intensity–modulated bend sensor by using a twin core fiber: Theoretical and experimental studies," *Opt. Exp.*, vol. 28, no. 10, pp. 14850–14858, May 2020, doi: 10.1364/OE.390054.

[23] J. He *et al.*, "Temperature–insensitive directional lateral force sensor based on dual side–hole fiber Bragg grating," *Opt. Exp.*, vol. 29, no. 12, pp. 17700–17709, Jun. 2021, doi: 10.1364/OE.415082.

[24] Y. J. Zhu, J. Zheng, H. C. Deng, L. B. Yuan, S. J. Deng, and C. X. Teng, "Refractive index and temperature measurement by cascading macro bending fiber and a sealed alternated SMF–MMF structure," *Opt. Commun.*, vol. 485, Apr. 2021, Art. no. 126738, doi: 10.1016/j.optcom.2020.126738.

[25] F. Wang, K. B. Pang, M. Tao, and X. Wang, "Folded–tapered multimode-no–core fiber sensor for simultaneous measurement of refractive index and temperature," *Opt. Laser Technol.*, vol. 130, Oct. 2020, Art. no. 106333, doi: 10.1016/j.optlastec.2020.106333.

[26] L. Duan, P. Zhang, M. Tang, R. X. Wang, D. M. Liu, and P. P. Shum, "Heterogeneous all–solid multicore fiber based multipath Michelson interferometer for high temperature sensing," *Opt. Exp.*, vol. 24, no. 18, pp. 20210–20218, Sep. 2016, doi: 10.1364/OE.24.020210.

[27] X. Quan and E. S. Fry, "Empirical equation for the index of refraction of seawater," *Appl. Opt.*, vol. 34, no. 18, pp. 3477–3480, May 1995, doi: 10.1364/AO.34.003477.